nature geoscience

Article

https://doi.org/10.1038/s41561-023-01298-w

Early Eocene low orography and high methane enhance Arctic warming via polar stratospheric clouds

Received: 17 December 2022

Accepted: 12 September 2023

Deepashree Dutta[1,2], Martin Jucker[1], Steven C. Sherwood[1], Katrin J. Meissner[1], Alex Sen Gupta[1] & Jiang Zhu[3]

Proxy data suggest that the early Eocene (~56–47.8 million years ago) was characterized by a much weaker equator-to-pole temperature gradient than today. However, general circulation models consistently underestimate high-latitude temperatures indicated by proxy records, suggesting that they may miss important processes. Previous studies hypothesized that wintertime polar stratospheric clouds may have played an important role in Arctic warming through greenhouse forcing, but these studies did not consider the effects of atmospheric chemistry or the early Eocene topography. Here we examine these factors using a high-top atmospheric model with interactive chemistry. The lower orography in the low- to mid-latitude Northern Hemisphere early Eocene weakens the stratospheric circulation which, in combination with sufficiently high methane concentrations, leads to a substantial increase in polar stratospheric clouds in the Arctic winter. Furthermore, an increase in early Eocene polar stratospheric clouds due to a 16- to 64-fold higher than pre-industrial methane concentration results in a radiative forcing larger than the direct greenhouse effect from the methane itself. This polar stratospheric cloud-induced radiative forcing could cause up to 7.4 K of Arctic surface warming. These results point to the potential for nonlinear interactions between individual forcings.

In the early Eocene, the Arctic was ice free with warmer average surface temperatures and a weaker seasonality than today[1–4]. Warm-temperate and temperate forests were abundant in the Northern Hemisphere high latitudes[5,6]. While the concentration of carbon dioxide (CO_2) was much higher (~1,500 parts per million by volume) than today[7], there are no proxies to constrain methane (CH_4) concentrations. Natural CH_4 in the atmosphere has both biogenic and geological sources. The dominant sink is due to the reaction of CH_4 with hydroxyl radicals in the atmosphere, with an additional small terrestrial biogenic sink. These sources and sinks are dependent on background climate and atmospheric composition. Previous modelling studies[8,9] suggest that atmospheric CH_4 concentrations might have been up to five times higher in the early Eocene compared to the pre-industrial period, but these studies did not include the chemical processes necessary to accurately simulate CH_4 sinks. An estimate of CH_4 emissions from the early Eocene wetlands was given by Wilton et al.[10] with a predictive algorithm using variables from the HadCM3BL-M2.2 model[11] and two different vegetation models. While they found a four–fivefold increase in terrestrial CH_4 emissions compared to the modern day, it is plausible that CH_4 surface fluxes were further elevated in the early Eocene due to large areas of

---

[1]Climate Change Research Centre and ARC Centre of Excellence for Climate Extremes, University of New South Wales, Sydney, New South Wales, Australia. [2]Department of Geography, University of Cambridge, Cambridge, United Kingdom. [3]Climate and Global Dynamics Laboratory, National Center for Atmospheric Research, Boulder, CO, USA. e-mail: dd643@cam.ac.uk

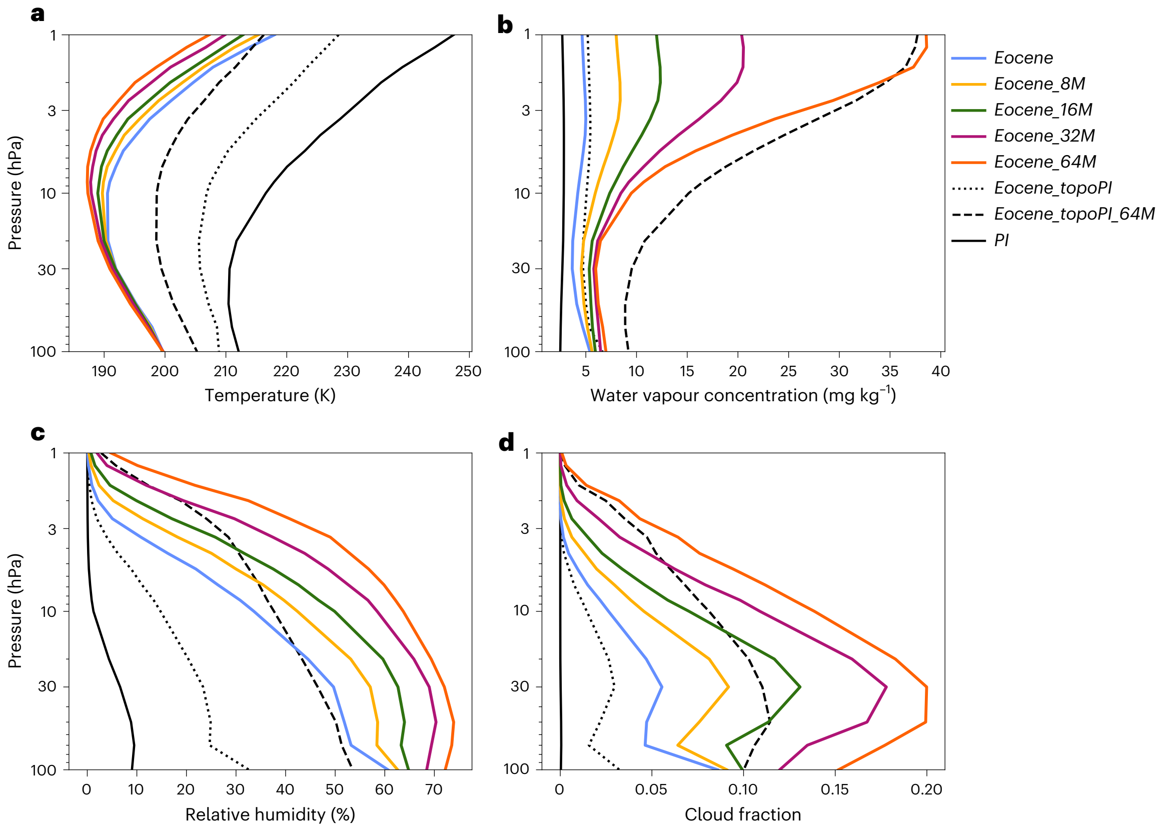

Fig. 1 | Arctic stratospheric temperature, water vapour concentration, relative humidity and cloud fraction. a–d, December–February mean temperature (**a**), water vapour concentration (**b**), relative humidity (**c**) and polar stratospheric cloud fraction (**d**) in the Arctic (area weighted mean between 70° N and 90° N) for different experiments (Extended Data Table 1).

forest[4], an enhanced hydrological cycle[12] and expansive shallow shelf seas[5,13], in particular in the southern Tethys and Arctic oceans. Earlier studies also suggested a nonlinear increase in the lifetime of CH_4 due to weaker sinks when concentrations of CH_4 are increased from modern values[14,15]. Hence CH_4 concentrations are highly uncertain in deep time. We therefore test a wide range of CH_4 concentrations in this study to explore the parameter space and evaluate possible consequences of concentrations within the higher end of the spectrum.

The continental arrangement and topography during the early Eocene were also considerably different from today (Extended Data Fig. 1). The Greenland ice sheet was absent[16] and many mountain chains were lower than today; for example, Greenland, which extends more than 2 km above sea level today, was only uplifted around 10–5 million years ago (Ma) (ref. 17). Similarly, the North American mountain ranges reached only ~2 km (ref. 18) and the Tibetan Plateau was less than 1 km above sea level[5,19] in the early Eocene compared with present day elevations of more than 3.5 km and 4.5 km, respectively. These differences in orography would affect the large-scale atmospheric circulation in the Northern Hemisphere by deflecting the atmospheric flow, thereby generating stationary Rossby waves[20]. Upward propagation and breaking of these waves can lead to changes in the large-scale stratospheric circulation, also known as the Brewer–Dobson circulation (BDC)[21]. The BDC influences the Arctic stratospheric temperature and the transport of water vapour, CH_4 and other trace gases into the stratosphere[22]. It therefore indirectly influences polar stratospheric clouds (PSCs) as they form when stratospheric temperature drops below a critical point in winter (~192–195 K) (ref. 23).

While the impact of present day orography[24], land–sea contrast[20] and sea surface temperatures (SSTs)[25] on the Northern Hemisphere winter stratospheric circulation has been widely studied, only one study has explored the stratosphere in the early Eocene[26]. For quadrupled CO_2 and higher than pre-industrial CH_4 and nitrous oxide, that modelling study suggested an increase in ozone concentration due to planetary waves in the early Eocene. It focused on the radiative effect of ozone in the early Eocene but did not investigate Arctic PSC changes or the role of topography.

PSCs trap the outgoing longwave radiation (OLR), thereby providing a greenhouse effect. They are not commonly observed in the present day Arctic due to a warm and highly variable polar vortex. However, a change in stratospheric temperature and composition in the early Eocene might have induced favourable conditions for Arctic PSC formation by cooling and/or moistening the Arctic stratosphere[27]. Here we examine this possibility using a stratosphere-resolving, fully interactive chemistry–climate atmosphere model with specified ocean temperatures. We assess the climate impact of CH_4 and PSC changes via the resulting changes in the top-of-atmosphere energy fluxes in our fixed-SST framework, indirectly inferring the Arctic warming that would result using an earlier study[28].

Formation of polar stratospheric clouds

Our baseline '*Eocene*' simulation is conducted with the early Eocene greenhouse gas (GHG) concentrations and surface boundary conditions[5], including the prescribed SSTs from a coupled simulation of the early Eocene[29]. A set of sensitivity experiments is then conducted by successively doubling the CH_4 concentration and changing the magnitude of polar amplification of SSTs (Extended Data Fig. 2). Another set of experiments, where topography is changed to its pre-industrial configuration while SSTs and GHG concentrations are held at *Eocene* values, is used to isolate the impact of topography (*Eocene_topoPI*). Extended Data Table 1 describes the experiments.

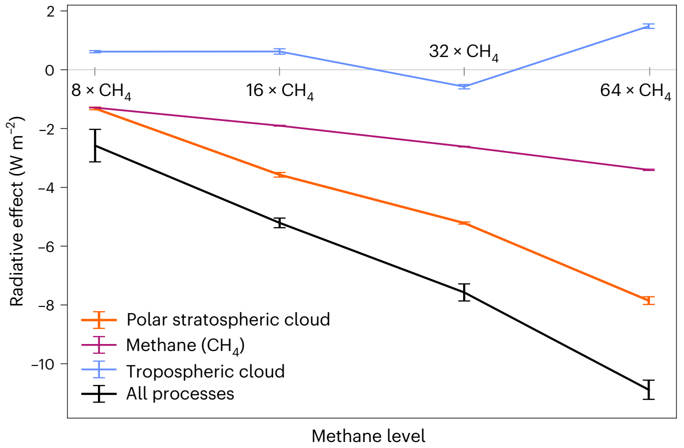

Fig. 2 | Radiative effects of polar stratospheric clouds, tropospheric clouds and methane in the Arctic. Difference in December–February mean outgoing longwave radiation for the early Eocene elevated methane experiments with respect to the 1 × methane early Eocene experiment (Extended Data Table 1). Radiative effects are obtained with a two-way partial radiative perturbation method using the parallel offline radiative transfer (PORT) model of the Community Earth System Model. 'Polar stratospheric cloud', 'Methane (CH$_4$)' and 'Tropospheric Cloud' show the individual radiative effects of polar stratospheric clouds, methane and tropospheric clouds. 'All Process' shows the difference in outgoing longwave radiation when all the physical processes are included in PORT. The error bars show standard error based on $n = 5$ winters.

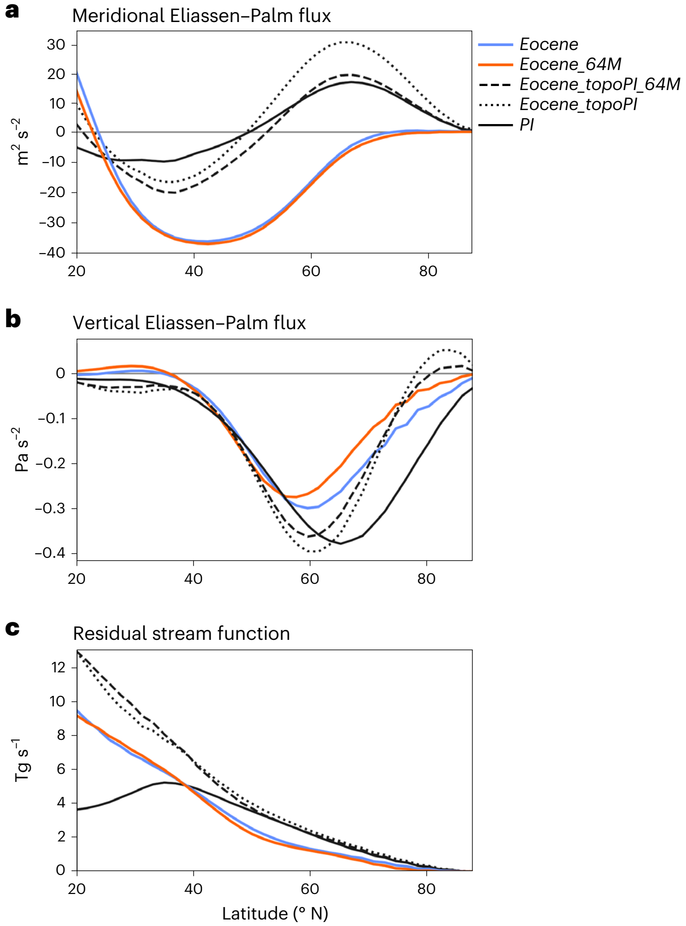

Fig. 3 | Eliassen–Palm and residual mean stream function at 70 hPa. **a**–**c**, December–February mean meridional (**a**) and vertical components (**b**) of Eliassen–Palm flux and residual mean stream function (**c**) for different experiments (Extended Data Table 1) for all zonal wavenumbers.

In the *Eocene* simulation, Arctic stratospheric temperatures are 15–30 K lower, which increases the likelihood of PSC formation compared to the pre-industrial control simulation (*PI*) (Fig. 1a). Comparison of the *Eocene*, *PI* and *Eocene_topoPI* experiments shows that most of the stratospheric cooling simulated for the early Eocene comes from the change in topography rather than SSTs (Fig. 1a); the cooling induced by the lower early Eocene orography is localized to the Arctic (Extended Data Fig. 3b). While there is minimal cooling associated with large increases in CH$_4$ concentration, there is a reduction in temperature of ~5 K in the stratosphere in *Eocene_topoPI_64M* relative to *Eocene_topoPI* (Fig. 1a), implying that the stratosphere is less sensitive to CH$_4$ in the early Eocene than in the pre-industrial atmosphere. By comparing *PI* with *Eocene_PItopo*, we see that elevated CO$_2$ and SST alone cause a zonally uniform cooling in the stratosphere (Extended Data Fig. 3d). An increase in polar amplified surface warming with early Eocene topography results in an increase in the Arctic stratospheric temperature compared with *Eocene* (Extended Data Fig. 4).

In addition to temperature, PSC formation also depends on the stratospheric water vapour concentration[30]. Two important mechanisms affecting the amount of water vapour entering the Arctic stratosphere are (1) CH$_4$ oxidation and (2) water vapour transiting the tropical tropopause, which is regulated largely by the tropical cold point temperature[31] but can be affected by cumulus clouds and aerosol concentrations in the tropics[32]. Consistent with the first mechanism, our simulations show increases in water vapour concentration in the Arctic stratosphere as CH$_4$ increases, irrespective of topography (Fig. 1b). In light of the second mechanism, we examined the tropical cold point temperature in the early Eocene and pre-industrial simulations (Extended Data Fig. 5a). In our experiments, the tropical cold point warms in response to warmer surface oceans and GHG concentrations, regardless of topography. Therefore, the water vapour that crosses the tropical tropopause is similar between *Eocene* and *Eocene_topoPI* (Extended Data Fig. 5b). Despite this, there is less water vapour in the Arctic stratosphere in *Eocene* (Fig. 1b). This can be explained by the Clausius–Clapeyron relation, that is, a reduction in the early Eocene stratospheric temperature reduces the water vapour concentration required to reach saturation and form clouds, dehydrating the polar stratosphere.

Our experiments highlight three main processes that may have been important for the formation of early Eocene PSCs: (1) a reduction in the Arctic stratospheric temperature associated with dynamical processes caused by the early Eocene topography, (2) radiative cooling due to an increase in GHGs and (3) possible CH$_4$-driven increases in water vapour concentration. Either a reduction in temperature or an increase in water vapour increases the relative humidity, thereby promoting PSC formation (Fig. 1c,d). While PSC fraction increases with relative humidity for both topographic configurations, for a given relative humidity increase, there is a smaller increase in PSC with the early Eocene compared with pre-industrial topography (Fig. 1c,d). The changes in the Arctic stratospheric temperature, water vapour and PSC fraction with different topography suggest differences in large-scale stratospheric dynamics between the early Eocene and pre-industrial simulations. Additionally we test the sensitivity to the early Eocene SST field by considering alternative cases of stronger polar amplification or globally uniform SST warming and find that Arctic PSCs increase compared to *PI* in each case but with varying amplitudes (Extended Data Fig. 4).

Impact of polar stratospheric clouds

Increases in PSCs and CH$_4$ both reduce the OLR, thereby causing greenhouse warming. To separate the radiative effects of PSCs, tropospheric clouds and CH$_4$ (Fig. 2), we used a two-way partial radiative perturbation

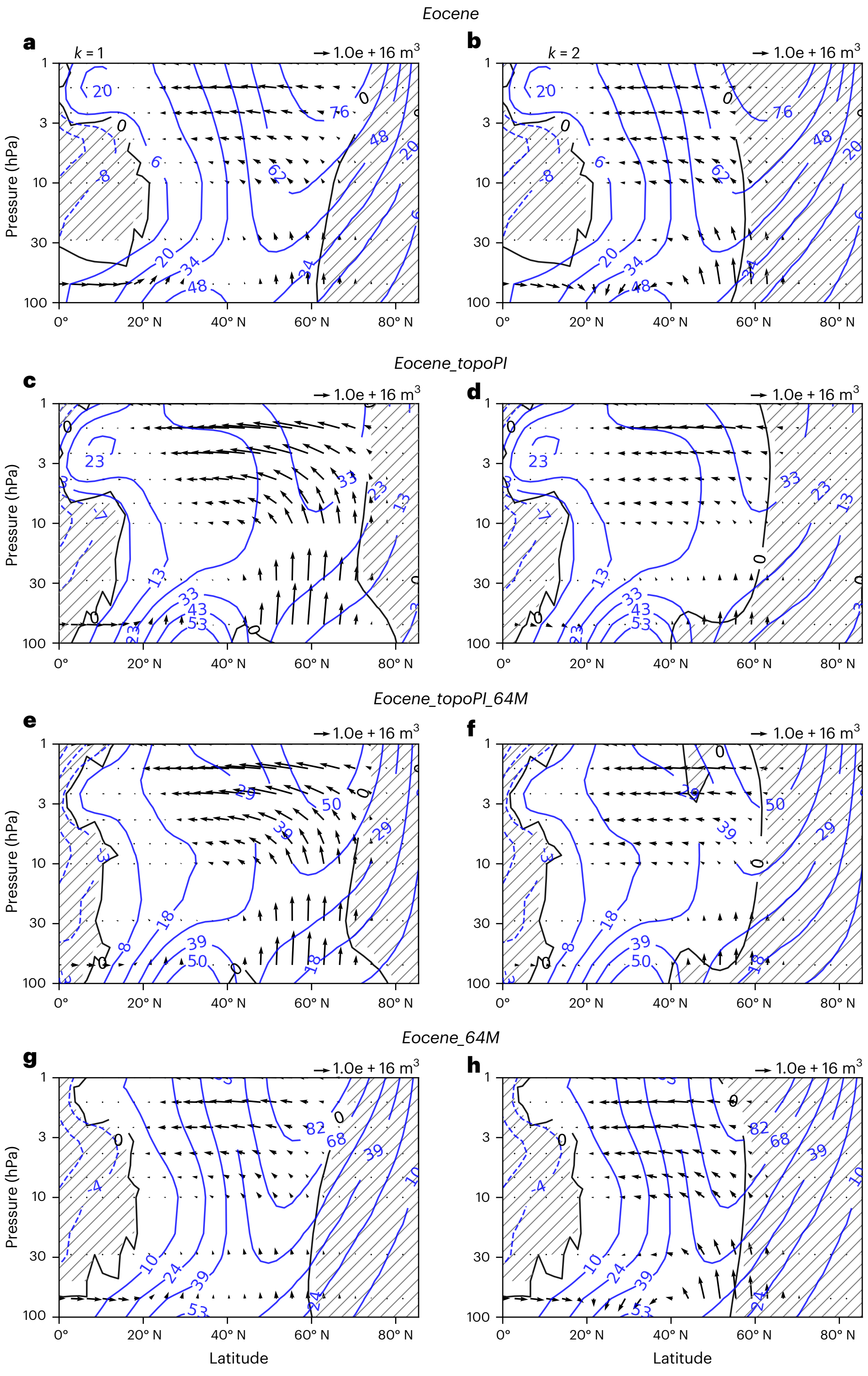

Fig. 4 | Wave propagation and wave-mean flow interaction. a–h, December–February mean Eliassen–Palm flux vectors[38] (in m^3) and zonal wind (in m s^{-1}, blue contours) for zonal wavenumbers $k = 1$ (left column) and $k = 2$ (right column) for the early Eocene (**a**,**b**,**g**,**h**) and pre-industrial (**c**–**f**) topography, with 1 × (**a**–**d**) and 64 × (**e**–**h**) methane concentrations, the early Eocene sea surface temperature and 6 × pre-industrial carbon dioxide concentrations. Areas with negative values of refractive index are shaded.

calculation with the parallel offline radiative transfer model (Methods). Under early Eocene conditions, increasing the CH$_4$ concentration by a factor of eight reduces the winter (December–February; DJF) OLR by ~2.5 W m^{-2} due to comparable contributions from PSCs and a direct radiative effect of CH$_4$ (Fig. 2). With additional increases in CH$_4$, the radiative effect of PSCs grows faster than that of the CH$_4$ direct forcing, becoming approximately twice as much at 32 × or 64 × pre-industrial CH$_4$ (Fig. 2). In our highest 64 × CH$_4$ early Eocene experiment, increased PSCs alone result in an OLR reduction of 7.85 W m^{-2} compared to the early Eocene 1 × CH$_4$ simulation. However, the same 64 × increase in

CH_4 with pre-industrial topography produces only a 2.92 W m^{-2} OLR reduction, suggesting that PSCs are unlikely to play an important role in Arctic amplification in the future.

Unlike PSCs, the column tropospheric cloud fraction in the Arctic remains similar despite the increases in CH_4 in the early Eocene simulations (Extended Data Fig. 6). Consequently, the OLR change due to tropospheric clouds is much smaller than that of PSCs in the high-CH_4 early Eocene experiments (Fig. 2).

As our experiments use prescribed SSTs, any additional surface warming related to enhanced radiative forcing would be largely constrained by the fixed boundary forcing. However, we can attempt to estimate the additional warming that would result from our simulated change in the Arctic OLR using a relationship between the extratropical heating anomaly and surface temperature change provided by Kang and Xie[28]. They imposed hemispherically symmetric polar heating anomalies in an aquaplanet mixed-layer ocean model coupled to an atmospheric model. In response to a steady heating of 18.47 W m^{-2} poleward of ±60°, they reported a near-surface air warming of 17.29 K over the Arctic and ~5 K in the tropics. Assuming the response scales linearly with forcing, and not taking into consideration any potential changes in ocean and atmospheric heat transports, we estimate that PSC radiative forcing would cause a wintertime Arctic surface temperature warming of 1.2 K, 3.3 K, 4.9 K and 7.4 K when CH_4 is increased by 8 ×, 16 ×, 32 × and 64 ×, respectively, in our early Eocene simulations, with much smaller changes in tropical temperatures. Applying this reasoning to annual mean PSC forcing (which is smaller than DJF mean) would result in a reduction of the annual mean equator-to-pole SST gradient ranging between 0.2 and 1.6 K and a global mean SST increase of 0.15–1.6 K across the 8 × to 64 × CH_4 experiments. If these perturbations are added to the coupled model SST means and gradients for the early Eocene simulated by Deep-Time Model Intercomparison Project models[33], the cluster of models comes closer to intersecting the observational band of 25–32 K mean and 14–22 K gradient (Extended Data Fig. 7). While this represents a very crude estimate of the impact of PSCs, which will be model dependent, it indicates that the PSCs at high CH_4 levels have the potential to improve overall model–proxy agreement.

Early Eocene topography drives polar stratospheric cloud formation

Insights into wave propagation and wave-mean flow interaction can be obtained from the Eliassen–Palm (EP) fluxes[34] (Fig. 3). In the early Eocene, there is an increase in the equatorward EP flux and a reduction in the upward EP flux poleward of ~20° N compared to the pre-industrial simulations (Fig. 3a,b). Reduced upward and enhanced equatorward EP flux results in an overall equatorward deviation of EP flux, which would otherwise propagate upwards into the upper stratosphere. The reduced flux reaching the polar regions leads to a reduction in the residual mean stream function poleward of 40° N (Fig. 3c) and reduced subsidence, that is, a weakening of the BDC (Extended Data Fig. 8) and its associated dynamical heating in the early Eocene compared to the pre-industrial simulations.

To investigate what drives these large differences in planetary wave propagation, we isolated the contributions of zonal wavenumbers 1 and 2 ($k = 1$ and $k = 2$) to the EP flux (Fig. 4). Waves with smaller wavenumber (longer wavelength) have a higher index of refraction and can propagate more easily into the stratosphere[35,36]. Additionally, planetary waves propagate away from regions of low refractive index towards high refractive index[35,36]. In general with the pre-industrial topography, $k = 1$ waves are dominant, resulting in a strong BDC. These long waves are mostly absent with lower early Eocene orography, however, leaving the EP flux at the base of the stratosphere to be dominated by $k = 2$ waves (Fig. 4), which mostly remain confined to the equatorward side of the polar vortex (Fig. 3a). The region of negative refractive index at high latitudes extends further southward in the early Eocene simulations with its $k = 2$ waves compared to the simulations with the pre-industrial topography (Fig. 4). Consequently, in the lower stratosphere poleward of ~60° N, planetary waves are refracted towards the tropics by the negative refractive index in the early Eocene (Fig. 4). By comparing the *Eocene*, *Eocene_64M* and *Eocene_topoPI* simulations, we can see that the shift in zonal wavenumber is due to the change in topography (Fig. 4). The lower topography therefore ultimately changes the upward and poleward propagation of waves (Fig. 4) and reduces the BDC strength in the early Eocene.

In contrast, comparison of *Eocene_topoPI* and *PI* suggests that surface warming increases the equatorward EP flux (Fig. 3a), strengthening the BDC southward of ~50° N (Fig. 3c). This indicates that surface warming mainly affects the equatorward branch of the BDC, while the low early Eocene orography weakens the poleward branch of the BDC. The associated weakening of the BDC reduces air descent in the Arctic, leading to an adiabatic cooling in the Arctic stratosphere and more PSCs due to lower temperatures.

In summary, we find that both a reduction in stratospheric temperature from the BDC weakening and an increase in water vapour concentration, due to higher CH_4 concentration, lead to a large increase in Arctic PSCs in the early Eocene. For a 16 × or greater increase in CH_4 concentration, the radiative impact of PSCs is approximately double that of the direct radiative effect of CH_4, producing a total longwave radiative forcing larger than ~5 W m^{-2} over the Arctic in wintertime. We estimate that in an early Eocene climate an increase in CH_4 concentration from 8 × to 64 × would lead to a surface warming of 1.2 K to 7.4 K. While the early Eocene CH_4 concentrations are highly uncertain, our study suggests that if CH_4 levels were much higher than today, an associated increase in PSC radiative forcing (and to a lesser extent, the direct effect of CH_4) could have resulted in substantial Arctic surface warming.

General circulation models that underestimate polar amplification in the early Eocene are not designed to adequately represent the stratospheric processes explored here[33]. Our simulations suggest that these processes, and in particular the ability to form PSCs, may be important for realistic Arctic warming. Both the lower orography that existed in the early Eocene and higher CH_4 concentrations that cannot be ruled out for that period, are favourable for PSC formation. Indeed, PSC formation is more sensitive to CH_4 changes with early Eocene topography and vice versa due to the reinforcing effects of lower temperatures and higher moisture in the lower stratosphere. Our study suggests that realistic simulation of stratospheric clouds might be an important missing process in climate models to explain past polar amplification. By extension we speculate that increases in topographic elevation since the early Eocene[5,37] might, via associated changes in stratospheric circulation and polar stratospheric clouds, be an additional factor in the observed slow cooling trend since that time, complementing the CO_2 reduction. However, confirming this would require further research. Given the higher modern orography, our results suggest that warming in the coming few centuries might not lead to as much polar amplification as suggested by the deep-time geological record.

Online content

Any methods, additional references, Nature Portfolio reporting summaries, source data, extended data, supplementary information, acknowledgements, peer review information; details of author contributions and competing interests; and statements of data and code availability are available at https://doi.org/10.1038/s41561-023-01298-w.

References

1. Inglis, G. N. et al. Global mean surface temperature and climate sensitivity of the early Eocene Climatic Optimum (EECO), Paleocene–Eocene Thermal Maximum (PETM), and latest Paleocene. *Clim* **16**, 1953–1968 (2020).
2. Greenwood, D. R. & Wing, S. L. Eocene continental climates and latitudinal temperature gradients. *Geology* **23**, 1044–1048 (1995).

3. Eberle, J. J. et al. Seasonal variability in Arctic temperatures during early Eocene time. *Earth Planet. Sci. Lett.* https://doi.org/10.1016/j.epsl.2010.06.005 (2010).
4. West, C. K. et al. Paleobotanical proxies for early Eocene climates and ecosystems in northern North America from middle to high latitudes. *Clim. Past* **16**, 1387–1410 (2020).
5. Herold, N. et al. A suite of early Eocene (~ 55 Ma) climate model boundary conditions. *Geosci. Model Dev.* https://doi.org/10.5194/gmd-7-2077-2014 (2014).
6. Eberle, J. J. & Greenwood, D. R. Life at the top of the greenhouse Eocene world—a review of the Eocene flora and vertebrate fauna from Canada's High Arctic. *Bull. Geol. Soc. Am.* **124**, 3–23 (2012).
7. Rae, J. W. B. et al. Atmospheric CO_2 over the past 66 million years from marine archives. *Annu. Rev. Earth Planet. Sci.* **49**, 609–641 (2021).
8. Beerling, D. J., Fox, A., Stevenson, D. S. & Valdes, P. J. Enhanced chemistry–climate feedbacks in past greenhouse worlds. *Proc. Natl. Acad. Sci. USA* https://doi.org/10.1073/pnas.1102409108 (2011).
9. Beerling, D., Berner, R. A., Mackenzie, F. T., Harfoot, M. B. & Pyle, J. A. Methane and the CH_4-related greenhouse effect over the past 400 million years. *Am. J. Sci.* **309**, 97–113 (2009).
10. Wilton, D. J. et al. A predictive algorithm for wetlands in deep time paleoclimate models. *Geosci. Model Dev.* **12**, 1351–1364 (2019).
11. Valdes, P. J. et al. The BRIDGE HadCM3 family of climate models: HadCM3@Bristol v1.0. *Geosci. Model Dev.* https://doi.org/10.5194/gmd-10-3715-2017 (2017).
12. Carmichael, M. J. et al. A model–model and data–model comparison for the early Eocene hydrological cycle. *Clim* **12**, 455–481 (2016).
13. Dong, Y. et al. Reconstruction of the early Eocene paleoclimate and paleoenvironment of the southeastern Neo-Tethys Ocean. *Glob. Planet. Change* **215**, 103875 (2022).
14. Stecher, L. et al. Slow feedbacks resulting from strongly enhanced atmospheric methane mixing ratios in a chemistry–climate model with mixed-layer ocean. *Atmos. Chem. Phys.* **21**, 731–754 (2021).
15. Winterstein, F., Tanalski, F., Jöckel, P., Dameris, M. & Ponater, M. Implication of strongly increased atmospheric methane concentrations for chemistry–climate connections. *Atmos. Chem. Phys.* **19**, 7151–7163 (2019).
16. Eldrett, J. S., Harding, I. C., Wilson, P. A., Butler, E. & Roberts, A. P. Continental ice in Greenland during the Eocene and Oligocene. *Nature* **446**, 176–179 (2007).
17. Steinberger, B., Spakman, W., Japsen, P. & Torsvik, T. H. The key role of global solid-Earth processes in preconditioning Greenland's glaciation since the Pliocene. *Terra Nova* **27**, 1–8 (2015).
18. Roy, M., Jordan, T. H. & Pederson, J. Colorado Plateau magmatism and uplift by warming of heterogeneous lithosphere. *Nature* **459**, 978–82 (2009).
19. Jian, X. et al. Late Cretaceous to early Eocene deformation in the northern Tibetan Plateau: detrital apatite fission track evidence from northern Qaidam basin. *Gondwana Res.* **60**, 94–104 (2018).
20. Garfinkel, C. I., White, I., Gerber, E. P., Jucker, M. & Erez, M. The Building Blocks of Northern Hemisphere Wintertime Stationary Waves. *J. Clim.* **33**, 5611–5633 (2020).
21. Brewer, A. W. Evidence for a world circulation provided by the measurements of helium and water vapour distribution in the stratosphere. *Q. J. R. Meteorol. Soc.* https://doi.org/10.1002/qj.49707532603 (1949).
22. Gerber, E. P. Stratospheric versus tropospheric control of the strength and structure of the Brewer–Dobson circulation. *J. Atmos. Sci.* **69**, 2857–2877 (2012).
23. Pitts, M. C., Poole, L. R. & Gonzalez, R. Polar stratospheric cloud climatology based on CALIPSO spaceborne lidar measurements from 2006 to 2017. *Atmos. Chem. Phys.* https://doi.org/10.5194/acp-18-10881-2018 (2018).
24. White, R. H., Battisti, D. S. & Roe, G. H. Mongolian mountains matter most: impacts of the latitude and height of asian orography on pacific wintertime atmospheric circulation. *J. Clim.* **30**, 4065–4082 (2017).
25. Olsen, M. A., Schoeberl, M. R. & Nielsen, J. E. Response of stratospheric circulation and stratosphere–troposphere exchange to changing sea surface temperatures. *J. Geophys. Res. Atmos.* **112**, D16104 (2007).
26. Szopa, S., Thiéblemont, R., Bekki, S., Botsyun, S. & Sepulchre, P. Role of the stratospheric chemistry–climate interactions in the hot climate conditions of the Eocene. *Clim* **15**, 1187–1203 (2019).
27. Sloan, L. C. & Pollard, D. Polar stratospheric clouds: a high latitude warming mechanism in an ancient greenhouse world. *Geophys. Res. Lett.* https://doi.org/10.1029/98GL02492 (1998).
28. Kang, S. M. & Xie, S. P. Dependence of climate response on meridional structure of external thermal forcing. *J. Clim.* **27**, 5593–5600 (2014).
29. Zhu, J., Poulsen, C. J. & Tierney, J. E. Simulation of Eocene extreme warmth and high climate sensitivity through cloud feedbacks. *Sci. Adv.* https://doi.org/10.1126/sciadv.aax1874 (2019).
30. Khosrawi, F. et al. Sensitivity of polar stratospheric cloud formation to changes in water vapour and temperature. *Atmos. Chem. Phys.* https://doi.org/10.5194/acp-16-101-2016 (2016).
31. Mote, P. W. et al. An atmospheric tape recorder: the imprint of tropical tropopause temperatures on stratospheric water vapor. *J. Geophys. Res. Atmos.* **101**, 3989–4006 (1996).
32. Sherwood, S. A microphysical connection among biomass burning, cumulus clouds, and stratospheric moisture. *Science* **295**, 1272–1275 (2002).
33. Lunt, D. et al. DeepMIP: model intercomparison of early Eocene climatic optimum (EECO) large-scale climate features and comparison with proxy data. *Clim. Past* https://doi.org/10.5194/cp-17-203-2021 (2021).
34. Eliassen, A. & Palm, E. On the transfer of energy in stationary mountain waves. *Geofys. Publ. Geophys. Norvegica* **22**, 1–23 (1960).
35. Matsuno, T. Vertical propagation of stationary planetary waves in the winter Northern Hemisphere. *J. Atmos. Sci.* **27**, 871–883 (1970).
36. Charney, J. G. & Drazin, P. G. Propagation of planetary-scale disturbances from the lower into the upper atmosphere. *J. Geophys. Res.* **66**, 83–109 (1961).
37. Zachos, J., Pagani, H., Sloan, L., Thomas, E. & Billups, K. Trends, rhythms, and aberrations in global climate 65 Ma to present. *Science* https://doi.org/10.1126/science.1059412 (2001).
38. Jucker, M. Scaling of Eliassen–Palm flux vectors. *Atmos. Sci. Lett.* **22**, e1020 (2021).

Methods

The Community Earth System Model (CESM) version 1.2.2[39] Whole Atmosphere Community Climate Model version 4 (WACCM4)[40] includes a fully interactive chemistry module based on the Model for Ozone and Related Chemical Tracers, version 3[41]. WACCM4 extends from the surface to 5.1×10^{-6} hPa (~140 km) with 66 vertical levels and has a horizontal resolution of 1.9° latitude by 2.5° longitude. Orographic gravity waves are parameterized based on surface roughness, while the parameterization of non-orographic gravity waves depend on frontal systems, the occurrence of deep convection and surface stress resulting from unresolved topography[40,42]. We used climatological SSTs as specified in the Extended Data Table 1. Solar parameters (for example, solar irradiance, wavelength) are based on an average climatology over the years 1834–1867, and the solar constant is set to 1,360 W m^{-2} following the DeepMIP protocol[43]. The 11-year solar cycle is not included. WACCM4 uses all of the physical parameterizations of the Community Atmospheric Model version 4 of CESM[39]. In our simulations, WACCM4 is coupled with the Community Land Model version 4.0 without dynamic vegetation or an active carbon–nitrogen cycle. Our simulations are integrated for a period of 60 years.

To test robustness, we conducted *Eocene* and *Eocene_64M* experiments with the Community Aerosol and Radiation Model for Atmospheres (CARMA) microphysical model coupled to WACCM4. The CARMA model is specifically developed to simulate PSCs[44–46]. Comparison of DJF mean clouds, water vapour concentration and atmospheric temperature between the WACCM4 simulations with and without CARMA showed very small difference in the Arctic stratosphere. Because WACCM4 coupled to CARMA is computationally expensive, we used WACCM4 without CARMA for the experiments reported.

Comparison of the free-running WACCM4 *PI* simulation with the European Centre for Medium-Range Weather Forecasts version 5 shows a warm bias of ~5 K poleward of 60°N between 100 and 10 hPa[47], which possibly causes an underestimation of PSCs. This bias is reduced in the specified dynamics version of WACCM4 with CARMA, which ultimately leads to better estimation of PSCs for today[44–46]. We use the free-running version of WACCM in this study as we do not have the reference fields of temperature, zonal and meridional winds and surface pressure in the early Eocene. The Quasi-Biennial Oscillation package is not activated in this study.

Idealized sensitivity experiments

To understand the sensitivity of PSCs to SST forcing, we conducted three additional idealized polar amplified SST experiments (Extended Data Fig. 2). The SSTs in these experiments are based on the Cloud Feedback Model Intercomparison Project (CFMIP) protocols (https://www.cfmip.org/experiments/informal-experiments; AMIP Polar Amplification) with the Eocene topography and 6 × pre-industrial CO_2 concentration. The SST anomaly added to the monthly varying pre-industrial control SST in *Pol20_EoTopo* is:

$$\mathrm{dSST} = 10 \times (1 - \cos(\pi \times \mathrm{latitude}/70^\circ))$$

In the second experiment we added a globally uniform 4 °C SST to *Pol20_EoTopo* (similar to the +4 K experiment of the Coupled Model Intercomparison Project phase 5/CFMIP2) to understand the role of SST warming while maintaining the same SST gradient as in *Pol20_EoTopo* (*Pol20_EoTopo_4K*). The third experiment (*Pol20_EoTopo_64M*) is based on *Pol20_EoTopo* but integrated with 64 × CH_4 concentration to understand the impact of a CH_4 increase in the presence of a reduced SST gradient. Extended Data Fig. 4 compares the results of these idealized sensitivity experiments with the *Eocene* and *PI* experiments.

Calculation of the radiative effects

To isolate the radiative effects of PSCs, tropospheric clouds and CH_4, we use the Parallel Offline Radiative Transfer (PORT) model of CESM. PORT calculates the top-of-the-atmosphere radiative fluxes offline using the same radiation code as WACCM4. Therefore, by individually changing the PSCs, tropospheric clouds or CH_4 concentration in PORT, we can isolate their radiative effect[47,48].

To assess the radiative effect of clouds and CH_4 in high-CH_4 early Eocene experiments, we replaced the variable under investigation in the early Eocene 1 × CH_4 experiment with that of the early Eocene high-CH_4 experiments and ran PORT offline (*RE_VAR_forward*). Therefore, a difference in OLR between *RE_VAR_forward* and the *Eocene* 1 × CH_4 experiment will only include the radiative effect of the variable under investigation. This is known as the forward partial radiative perturbation (PRP) or one-sided PRP. Earlier studies show that use of the one-sided PRP technique might result in errors as radiative flux changes depend on background state[49,50]. Therefore, we also conduct a reverse PRP in which we use the high-CH_4 early Eocene climates as a baseline and replace the PSCs, tropospheric clouds and CH_4 one by one, with the variable values from the *Eocene* 1 × CH_4 experiment (*RE_VAR_reverse*). Then, following the same procedure as in the forward PRP, we calculate the difference in the OLR between *RE_VAR_reverse* and the respective high-CH_4 early Eocene experiment. Finally, we present the average OLR change obtained from the forward and reverse PRP techniques. We run the offline radiation code for the last five years of WACCM4 simulation.

As we are interested in the radiative impact associated with stratospheric changes, we allow the dynamical heating of the stratosphere to respond to surface warming or greenhouse gas emissions in the PORT offline radiation calculations. We also calculated the radiative effects of PSCs and CH_4 in the *Eocene_64M* experiment with the fixed dynamical heating approach, in which the stratospheric temperatures are adjusted to radiative equilibrium. We find that the fixed dynamical heating approach results in a small additional OLR reduction due to PSCs and CH_4 of 0.47 W m^{-2} and 0.3 W m^{-2}, respectively, from that of the PORT calculations with stratospheric dynamical heating.

Data availability

Model outputs can be downloaded from https://doi.org/10.6084/m9.figshare.23690946.

Code availability

Dynamical analysis was performed with the help of the aostools package available at https://github.com/mjucker/aostools. The WACCM4 model code is available at the National Center for Atmospheric Research software development repository (https://svn-ccsm-models.cgd.ucar.edu/cesm1/exp_tags/pcesm_cesm1_2_2_tags/dt-cesm1.0_cesm1_2_2_1/).

References

39. Hurrell, J. W. et al. The community earth system model: a framework for collaborative research. *Bull. Am. Meteorol. Soc.* **94**, 1339–1360 (2013).
40. Marsh, D. R. et al. Climate change from 1850 to 2005 simulated in CESM1(WACCM). *J. Clim.* **26**, 7372–7391 (2013).
41. Kinnison, D. E. et al. Sensitivity of chemical tracers to meteorological parameters in the MOZART-3 chemical transport model. *J. Geophys. Res. Atmos.* **112**, D20302 (2007).
42. Richter, J. H., Sassi, F. & Garcia, R. R. Toward a physically based gravity wave source parameterization in a general circulation model. *J. Atmos. Sci.* **67**, 136–156 (2010).
43. Lunt, D. J. et al. The DeepMIP contribution to PMIP4: experimental design for model simulations of the EECO, PETM, and pre-PETM (version 1.0). *Geosci. Model Dev.* https://doi.org/10.5194/gmd-10-889-2017 (2017).
44. Zhu, Y. et al. Development of a polar stratospheric cloud model within the Community Earth System Model: assessment of 2010 Antarctic winter. *J. Geophys. Res. Atmos.* **122**, 10,418–10,438 (2017).

45. Zhu, Y. et al. Comparing simulated PSC optical properties with CALIPSO observations during the 2010 Antarctic winter. *J. Geophys. Res.* **122**, 1175–1202 (2017).
46. Zhu, Y. et al. Development of a polar stratospheric cloud model within the Community Earth System Model using constraints on Type I PSCs from the 2010–2011 Arctic winter. *J. Adv. Model. Earth Syst.* **7**, 551–585 (2015).
47. Dutta, D., Sherwood, S. C., Jucker, M., Gupta, A. S. & Meissner, K. J. Can polar stratospheric clouds explain Arctic amplification? *J. Clim.* **36**, 2313–2332 (2022).
48. Conley, A. J., Lamarque, J. F., Vitt, F., Collins, W. D. & Kiehl, J. PORT, a CESM tool for the diagnosis of radiative forcing. *Geosci. Model Dev.* **6**, 469–476 (2013).
49. Soden, B. J. et al. Quantifying climate feedbacks using radiative kernels. *J. Clim.* **21**, 3504–3520 (2008).
50. Colman, R. A. & McAvaney, B. J. A study of general circulation model climate feedbacks determined from perturbed sea surface temperature experiments. *J. Geophys. Res. Atmos.* **102**, 19383–19402 (1997).

Acknowledgements

We acknowledge the support from the Australian Research Council (CE170100023, D.D., M.J., S.C.S., K.J.M., A.S.G; FL150100035, S.C.S.; DP180100048, K.J.M.) and the Australian Government Research Training Program Scholarship (D.D). Computational resources were provided by the National Computational Infrastructure (NCI) National Facility at the Australian National University through awards under the Merit Allocation Scheme and the University of New South Wales high-performance computing (HPC) at NCI Scheme. The CESM project is supported primarily by the US National Science Foundation (NSF). This material is based upon work supported by the National Center for Atmospheric Research, which is a major facility sponsored by the NSF under cooperative agreement number 1852977. We thank C. K. West and the other anonymous reviewers for valuable suggestions.

Author contributions

D.D., K.J.M., S.C.S., M.J. and A.S.G. developed the concept of the paper. D.D. set up the WACCM4 experiments with support from J.Z. D.D. performed the analysis, literature assessment and the initial draft of the manuscript. All the authors contributed to the discussion of the results and compilation of the paper.

Competing interests

The authors declare no competing interests.

Additional information

Extended data is available for this paper at https://doi.org/10.1038/s41561-023-01298-w.

Supplementary information The online version contains supplementary material available at https://doi.org/10.1038/s41561-023-01298-w.

Correspondence and requests for materials should be addressed to Deepashree Dutta.

Peer review information *Nature Geoscience* thanks Christopher West and the other, anonymous, reviewer(s) for their contribution to the peer review of this work. Primary Handling Editor: James Super, in collaboration with the *Nature Geoscience* team.

https://doi.org/10.1038/s41561-023-01298-w

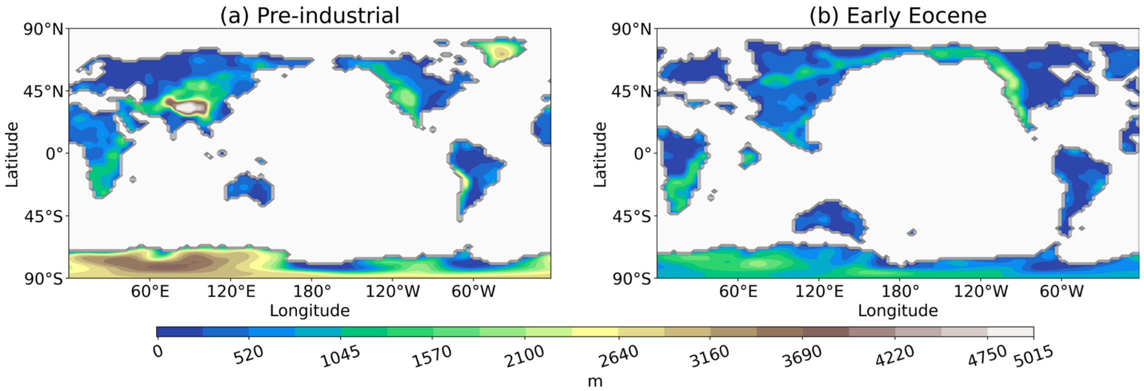

Extended Data Fig. 1 | Orography maps. Orography of pre-industrial (**a**) and early Eocene (**b**).

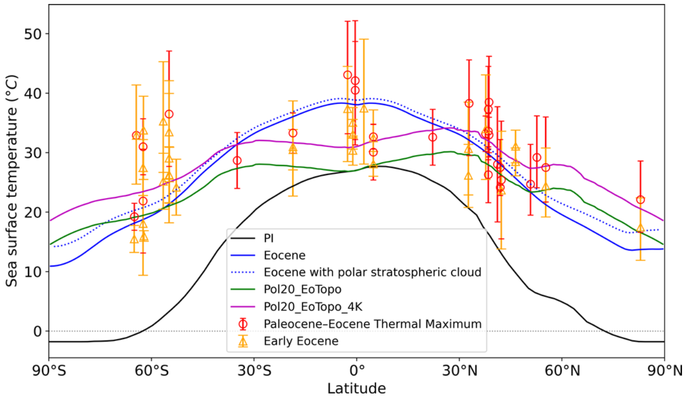

Extended Data Fig. 2 | Model-data comparison for the early Eocene sea surface temperature (SST). Annual mean SST in *PI*, *Eocene*, *Pol20_EoTopo*, and *Pol20_EoTopo_4K* experiments in black, blue, green, and magenta lines, respectively. The dotted blue line shows the annual mean *Eocene* SST plus the polar stratospheric cloud induced warming estimated using the linearly scaled Kang and Xie[1] results. More details about these experiments can be found in the Idealized Sensitivity Experiment section of the Methods. Yellow and red dots show the SST proxies for the Eocene and Paleocene– Eocene Thermal Maximum from the compilation by Zhu et al.[2]. For details of the sites, core name, location, proxy type, calculation method, uncertainty quantification, and references please refer to the supplementary document of Zhu et al.[2].

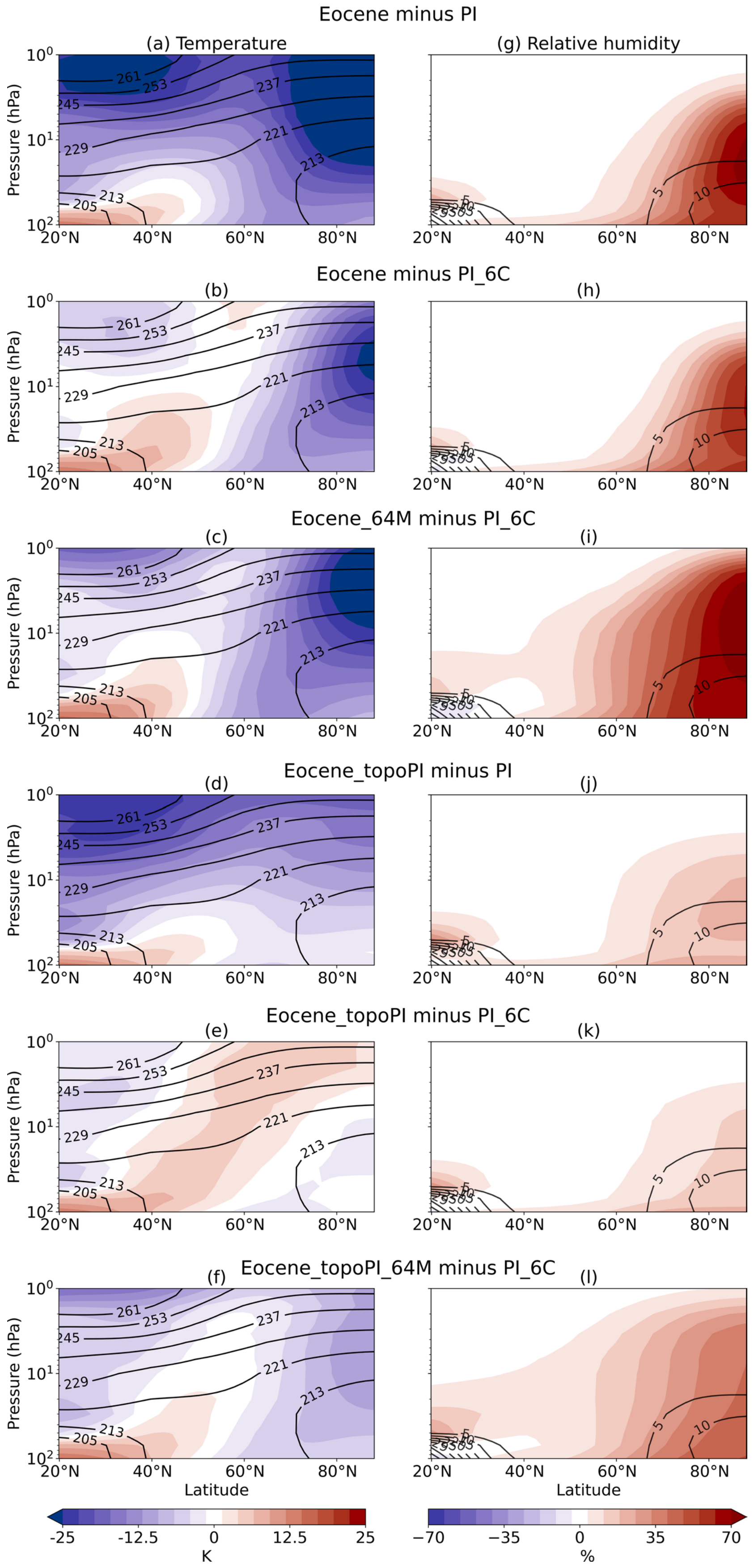

Extended Data Fig. 3 | Temperature and relative humidity change. a–l, December-February mean temperature and relative humidity change between different experiments (Extended Data Table 1) in (**a–f**) and (**g–l**), respectively.

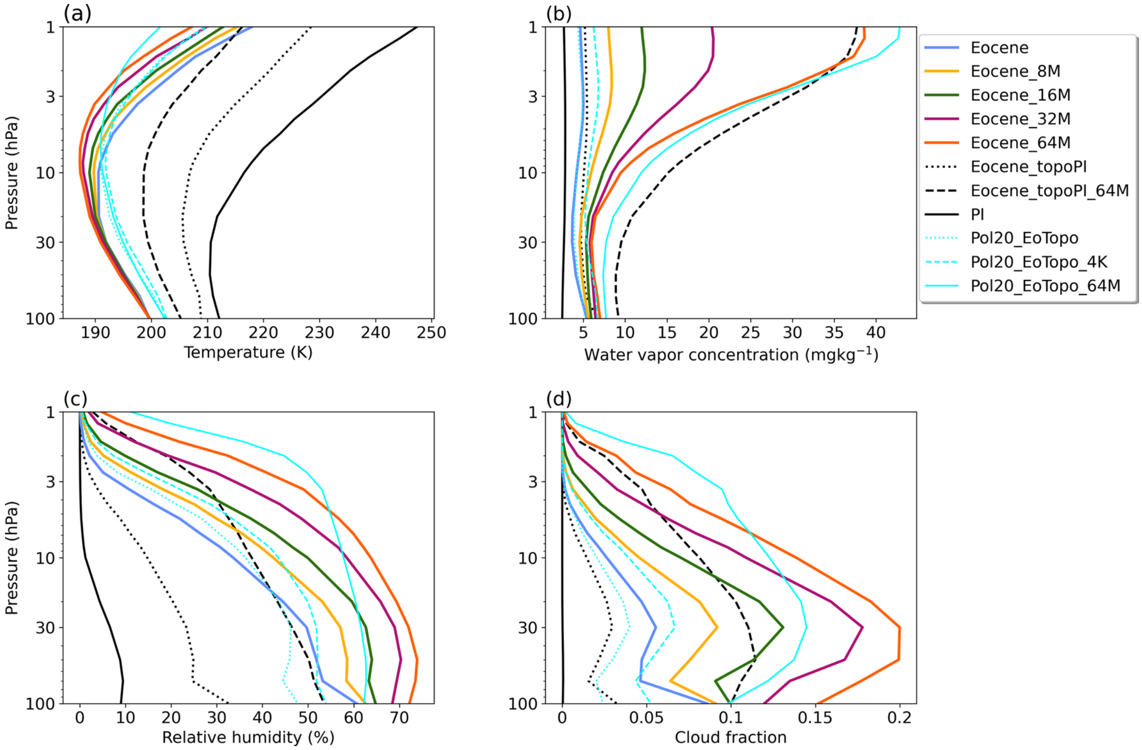

Extended Data Fig. 4 | Arctic stratospheric temperature, water vapour concentration, relative humidity, and cloud fraction. a–**d**, December-February mean temperature (**a**), water vapour concentration (**b**), relative humidity (**c**) and cloud fraction (**d**) in the Arctic (area weighted mean between 70°N- 90°N) for different experiments (Extended Data Table 1). *Pol20_EoTopo* is integrated with an idealized polar amplified sea surface temperature (SST) with 6 × pre- industrial carbon dioxide concentration and the early Eocene topography. In the *Pol20_EoTopo_4K* experiment, a uniform SST of 4 °C is added globally to *Pol20_EoTopo*. Methane concentration is increased by 64 × in *Pol20_EoTopo_64M* while keeping everything else the same as *Pol20_EoTopo*. More details about these experiments can be found in the Idealized Sensitivity Experiment section of the Methods.

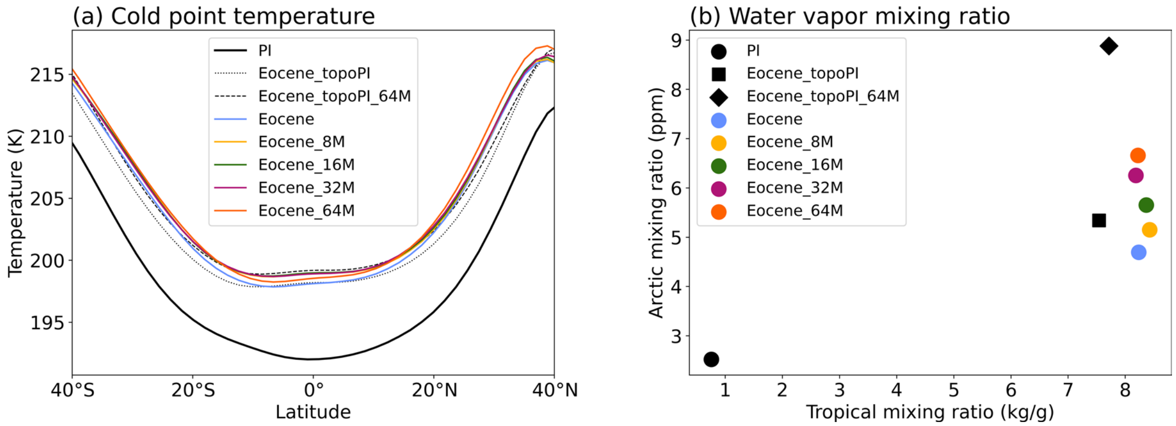

Extended Data Fig. 5 | Tropical cold point temperature and water vapour transport. a–b, December-February mean cold point temperature (**a**), water vapor mixing ratio (**b**) in the Arctic (area weighted mean between 70°N-90°N) and tropics (between 12°N- 12°S) for different experiments (Extended Data Table 1).

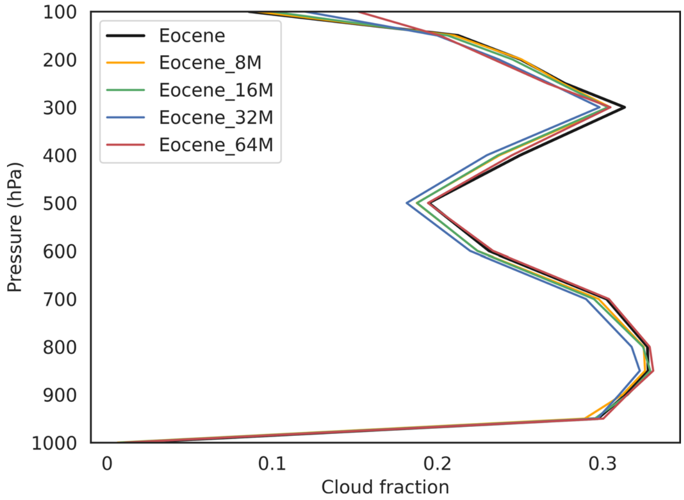

Extended Data Fig. 6 | Arctic tropospheric cloud fraction. December-February mean tropospheric cloud fraction in the Arctic (area weighted mean between 70°N-90°N) for different early Eocene simulations (Extended Data Table 1).

https://doi.org/10.1038/s41561-023-01298-w

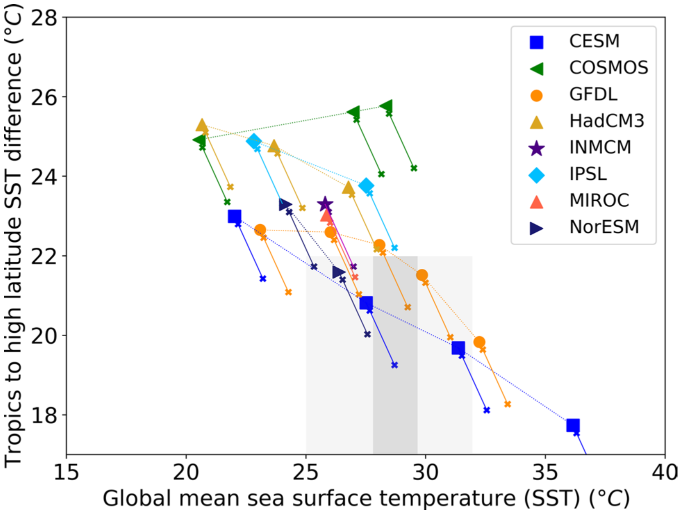

Extended Data Fig. 7 | Improvements in model-proxy agreement associated with polar stratospheric clouds. Annual mean meridional sea surface temperature (SST) gradient (average SST equatorward of ±30° minus average SST poleward of ±60°) as a function of global mean SST for the Deep-Time Model Intercomparison Project simulations. Different markers of the same symbol and colour show simulations with the same model and different carbon dioxide concentrations. The light and dark grey boxes show meridional SST gradient and global mean SST reconstructed from proxy data (10% to 90% and 33% to 66% confidence intervals, respectively). The lines extending downwards from filled dots to the crosses highlight the estimated reduction in annual mean SST gradient and increase in annual and global mean SST caused by polar stratospheric cloud induced warming. Figure reproduced from Fig. 1b in Lunt et al.[3].

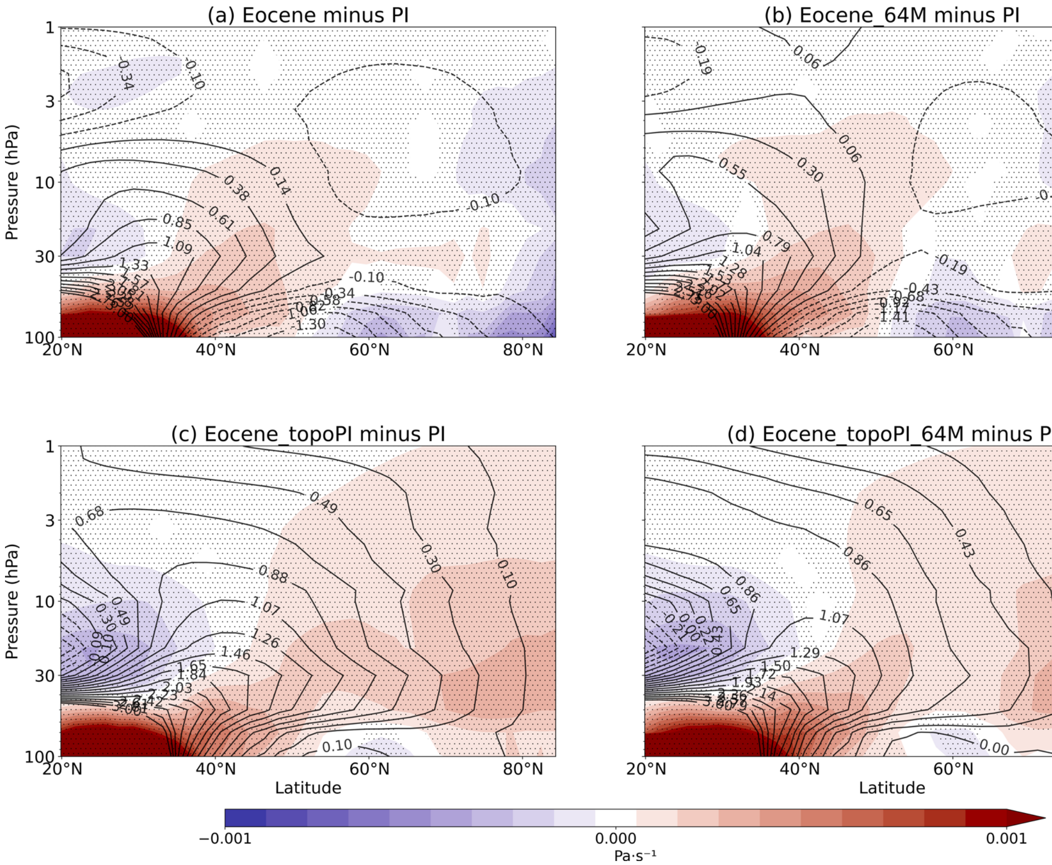

Extended Data Fig. 8 | Residual mean vertical velocity and transformed Eulerian-mean circulation. a–d, December-February mean changes in residual mean vertical velocity (in Pa s^{-1}, shading) and transformed Eulerian-mean circulation (in 10^9 kg s^{-1}, contours) in *Eocene* minus *PI* (**a**), *Eocene_64M* minus *PI* (**b**), *Eocene_topoPI* minus *PI* (**c**), and *Eocene_topoPI_64M* minus *PI* (**d**), respectively. Stippling in the plots shows regions where differences in vertical velocity are statistically significant ($p < 0.05$). Details about the experiments can be found in the Extended Data Table 1.

Extended Data Table 1 | List of experiments

Experiment	Sea surface temperature (SST) and sea ice	Continental arrangement and orography	Carbon dioxide (CO_2)	Methane (CH_4)	Goal
Eocene	Monthly-varying climatological SSTs from the coupled Eocene experiment of Zhu et al.[2]	Same as Herold et al.[4]	6 × pre-industrial (PI)	PI	Use as a reference for high CH_4 early Eocene simulations. Assess the Brewer-Dobson circulation (BDC) strength and Arctic polar stratospheric clouds (PSCs) compared to PI
Eocene_8M	Same as *Eocene*	Same as *Eocene*	6 × PI	8 × PI	Assess the impact of CH_4 increase on PSCs. Provide a comparative analysis of radiative effects of PSCs and CH_4
Eocene_16M				16 × PI	
Eocene_32M				32 × PI	
Eocene_64M				64 × PI	
PI	Monthly-varying climatological PI SST and sea ice from Hurrell et al.[5]	PI	PI	PI	Use as a reference for the experiments with PI topography
Eocene_topoPI	Same as *Eocene*	PI	6 × PI	PI	Difference from *Eocene* shows the impact of topography change. Difference from *PI* shows the combined impacts of SST and CO_2 change
Eocene_topoPI_64M	Same as *Eocene*	PI	6 × PI	64 × PI	Role of CH_4 increase on PSCs for PI topography
Pol20_EoTopo	Idealized polar amplified SST as described in *Methods*	Same as *Eocene*	6 × PI	PI	Comparison with *Eocene* shows the impact of stronger polar amplification on PSCs
Pol20_EoTopo_4K	*Pol20_EoTopo* plus 4K	Same as *Eocene*	6 × PI	PI	Comparison with *Pol20_EoTopo* clarifies the role of SST warming
Pol20_EoTopo_64M	Same as *Pol20_EoTopo*	Same as *Eocene*	6 × PI	64 × PI	Comparison with *Pol20_EoTopo* clarifies the impact of CH_4 increase